Strongly correlated electron behavior in a new member of the $A_{n+1}B_nX_{3n+1}$ homologous series: Ce$_7$Co$_6$Ge$_{19}$

Ashley Weiland [1], Kaya Wei [2,3] Gregory T. McCandless,[1] Justin B. Felder,[1] Lucas J. Eddy [1],
Ryan E. Baumbach,[2,3] and Julia Y. Chan [1],[*]

[1]*Department of Chemistry & Biochemistry, University of Texas at Dallas, Richardson, Texas 75080, USA*
[2]*National High Magnetic Field Laboratory, Florida State University, Tallahassee, Florida 32310, USA*
[3]*Department of Physics, Florida State University, Tallahassee, Florida 32306, USA*

While f-electron intermetallics are well-known as hosts for complex valence behavior, magnetism, and unconventional superconductivity, it remains a persistent challenge to design specific phenomena. Some guidance is provided by studies of large families of materials, such as those based on the AlB$_2$, AuCu$_3$, and BaAl$_4$ structural subunits, where systematic trends in their electronic behavior have been observed. This suggests that an effective approach in developing designer materials is to incorporate multimodal stacking arrangements of well-understood building blocks. Here, we report results for Ce$_7$Co$_6$Ge$_{19}$, the $n = 6$ member of a new homologous series, $A_{n+1}B_nX_{3n+1}$, that consists of subunits previously identified as having potential for unconventional magnetic behavior. We show that Ce$_7$Co$_6$Ge$_{19}$ exhibits complex magnetism with evidence for frustration and Kondo lattice behavior that is directly related to what is seen in other n value analogs. Here, the added structural units introduce additional magnetic degrees of freedom, demonstrating that it is possible to rationally design magnetic complexity, and possibly other phenomena in this family of intermetallics.

I. INTRODUCTION

The general concept that exotic behavior is generated by competition or cooperation between (i) complex magnetic interactions and (ii) hybridization between f- and conduction-electron states has become foundational for understanding the physics of strongly correlated electron metals [1,2]. This is exemplified in certain subsets of materials, such as those that include Ce, Yb, U, Np, and Pu, and that feature specific irreducible crystalline building blocks, such as AuCu$_3$ and BaAl$_4$ [3]. For instance, the family that is based on CeIn$_3$ (AuCu$_3$-type structure) shows remarkable behavior that spans from heavy fermion antiferromagnetism in CeRhIn$_5$ [4] and CePt$_2$In$_7$ [5], to magnetic quantum criticality with unconventional superconductivity for CeCoIn$_5$ [6], to unconventional superconductors whose Cooper pairing mechanism remains almost completely unknown in PuCoGa$_5$ [7] and NpPd$_5$Al$_2$ [8]. Each one of these examples features the AuCu$_3$-like subunit, which is then layered between different stacking arrangements of other elements. This suggests that a powerful approach for designing attractive behaviors is to develop f-electron materials with analogous structural flexibility.

Ce$_7$Co$_6$Ge$_{19}$ is a new member of the homologous series, $A_{n+1}B_nX_{3n+1}$, where A is a rare earth metal, B is a transition metal, and X is a tetrel (Group 14 element) [9]. The $A_{n+1}B_nX_{3n+1}$ homologous series consists of members whose structures are built by substructural units with the greatest potential for unconventional magnetic behavior, such

as AlB$_2$, AuCu$_3$, and BaAl$_4$ structure types with prominent examples of highly correlated behavior. Although the series is chemically versatile, here we primarily focus on Ce-Co-Ge combinations/subunits. The $n = 1$ member, Ce$_2$CoGe$_4$ (also written CeCo$_{0.5}$Ge$_2$), crystallizes in the CeNiSi$_2$ structure type [10], and the nonstoichiometric CeCo$_{0.89}$Ge$_2$ exhibits a slightly enhanced electron mass [11]. Ce$_3$Co$_2$Ge$_7$ ($n = 2$), though not yet reported, can be ascribed to the La$_3$Co$_2$Sn$_7$ structure type [12], which consists of two CeCoGe$_2$ units capping one CeGe$_3$ (AuCu$_3$ type) unit. Several analogs of the $n = 2$ structure type are well studied, including Ce$_3$Ni$_2$X$_7$ ($X =$ Ge, Sn) [13,14], and Ln_3Co$_{2+x}$Ge$_7$ ($Ln =$ Pr, Nd, Sm) [15]. Ce$_4$Co$_3$Ge$_{10}$ ($n = 3$) has not yet been reported, though Eu$_4$Ni$_3$Sn$_{10}$ [16] is considered as part of the series, as the structure consists of EuSn$_3$ (AuCu$_3$ type) units between inverted noncentrosymmetric EuNiSn$_3$ (BaNiSn$_3$ type) units. Ce$_5$Co$_4$Ge$_{13}$ ($n = 4$) [17] can be described as an intergrowth of the CeGe$_3$ (AuCu$_3$ type) unit, i.e., [CeCoGe$_3$ – CeGe$_3$ – CeCoGe$_3$] – CeGe$_3$ – [CeCoGe$_3$ – CeGe$_3$ – CeCoGe$_3$] where the order in square brackets is the same as the $n = 3$ structure. The structure of $n = 5$ [18], similar to $n = 4$, contains two disordered cuboctahedral slabs instead of the one ordered CeGe$_3$ (AuCu$_3$ type) slab.

Herein, we report the flux crystal growth, structural, and electronic/magnetic properties of the new $n = 6$ member of the $A_{n+1}B_nX_{3n+1}$ homologous series: Ce$_7$Co$_{6+x}$Ge$_{19-y}$Sn$_y$, where Ce$_7$Co$_6$Ge$_{19}$ will be used throughout the manuscript for simplicity. Similar to that of the $n = 5$ analog [18], this compound exhibits complex magnetism with evidence for frustration and Kondo lattice hybridization. As expected from the building-block paradigm, the added structural units

---

*Corresponding author: Julia.Chan@utdallas.edu
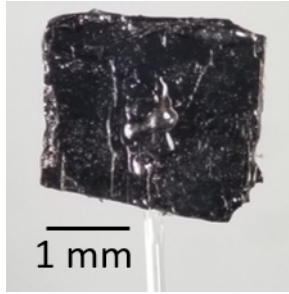
FIG. 1. A photograph of the $Ce_7Co_6Ge_{19}$ crystal used in properties measurements.

introduce additional magnetic degrees of freedom demonstrating the relatively straightforward potential to rationally design magnetic complexity.

II. MATERIALS AND METHODS

A. Synthesis

A ratio of 5Ce:4Co:13Ge was arc melting three times, flipping sides for homogeneity. The resulting button was broken into pieces and combined with 12 molar excess (with respect to Ce) of Sn flux in a Canfield crucible set [19]. The crucibles were sealed under $\sim$1/3 atm of Ar gas in a fused silica tube. The reaction was placed in a furnace at 300 °C, heated to 1000 °C at 100 °/h, held for 48 h, and cooled to 815 °C at a rate of 2 °/h. The tube was then removed from the furnace and inverted into a centrifuge to remove the excess molten tin. The crystals were partially coated with trace amounts of Sn flux, which was removed by etching with HCl and water (1:1 ratio). The resulting metallic-silver plates vary in size from $\sim$0.1 mm

TABLE I. Crystal data, data collection, and refinement parameters.

Formula	$Ce_7Co_{6.51}Ge_{18.50}Sn_{0.50}$
Space Group	*Cmmm*
a (Å)	4.3156(13)
b (Å)	65.33(2)
c (Å)	4.3302(14)
V(Å^3)	1220.8(7)
Z	2
Temperature (K)	298
θ range (deg)	5.0–36.4
μ(mm^{-1})	39.87
Measured reflns	28145
Independent reflns	1817
R_{int}	0.099
h	$-7-7$
k	$-108-108$
l	$-7-7$
$\Delta\rho_{max}$ (Å^{-3})	6.15
$\Delta\rho_{min}$ (Å^{-3})	-9.18
GOF	1.12
Extinction coefficient	0.00022(3)
R_1 ($F^2 > 2\sigma(F^2)$)	0.086
$wR_2(F^2)$	0.177

TABLE II. Fractional atomic coordinates.

Atom	x	y	z	Occ (<1)	U_{eq} (Å^2)
Ce1	0	0.27589(2)	½		0.0073(3)
Ge1B	0	0.23824(4)	0		0.0067(4)
Co1C	0	0.20193(5)	0		0.0045(5)
Ce2	0	0.42435(2)	½		0.0080(3)
Sn2A	0	0.0751(3)	0	0.120(6)	0.0120(5)
Ge2B	0	0.08604(5)	0	0.880(6)	0.0120(5)
Co2C	0	0.05133(6)	0	0.880(6)	0.0120(5)
Ce3	0	0.15112(2)	0		0.0053(2)
Ge3B	0	0.33867(4)	½		0.0064(4)
Co3C	0	0.37361(5)	½		0.0050(5)
Ce4	0	0	0		0.0105(4)
Sn4A	0	½	½	0.253(9)	0.0181(12)
Ge4B	0	0.48938(15)	½	0.373(4)	0.0181(12)
Co4C	0	0.47651(18)	½	0.373(4)	0.0181(12)
Ge5	0	0.18732(4)	½		0.0080(5)
Ge6	0	0.31256(4)	0		0.0067(5)
Ge7	0	0.38790(4)	0		0.0081(5)
Ge8	0	0.11208(4)	½		0.0070(5)
Ge9	0	0.03706(4)	½		0.0111(5)
Ge10	0	0.46288(4)	0		0.0111(5)

single crystals to $\sim$1 cm clusters of plates. A typical single crystal is shown in Fig. 1.

B. Single-crystal X-ray diffraction

A single crystal of size $0.02 \times 0.05 \times 0.10$ mm was selected and data were collected on a Bruker D8 Quest diffractometer with an Incoatec microfocus source (IμS, Mo K$_\alpha$ radiation, $\lambda = 0.71073$ Å) and a PHOTON II CPAD area detector. The raw data frames were reduced using the Bruker SAINT software, and a multiscan absorption correction was applied with Bruker SADABS [20]. An initial structural model was obtained with the intrinsic phasing feature of SHELXT [21], and least-squares refinements were performed with SHELXL2014 [22]. Table I gives data collection and refinement statistics, Table II provides fractional atomic coordinates, and Table III gives selected Ce-Ce interatomic distances.

C. Magnetic and physical properties measurements

Magnetization measurements were carried out using single crystals at temperatures $T = 1.8$–300 K under an applied magnetic field of $H = 0.1$ T for H applied parallel to the a, b, and c axes using a Quantum Design vibrating sample magnetometer magnetic property measurement system. The

TABLE III. Selected shortest Ce-Ce interatomic distances.

Atoms	Distance (Å)
Ce1 – Ce1	4.0124(18)
Ce2 – Ce2	4.3156(13)
Ce3 – Ce3	4.3156(13)
Ce4 – Ce4	4.3156(13)
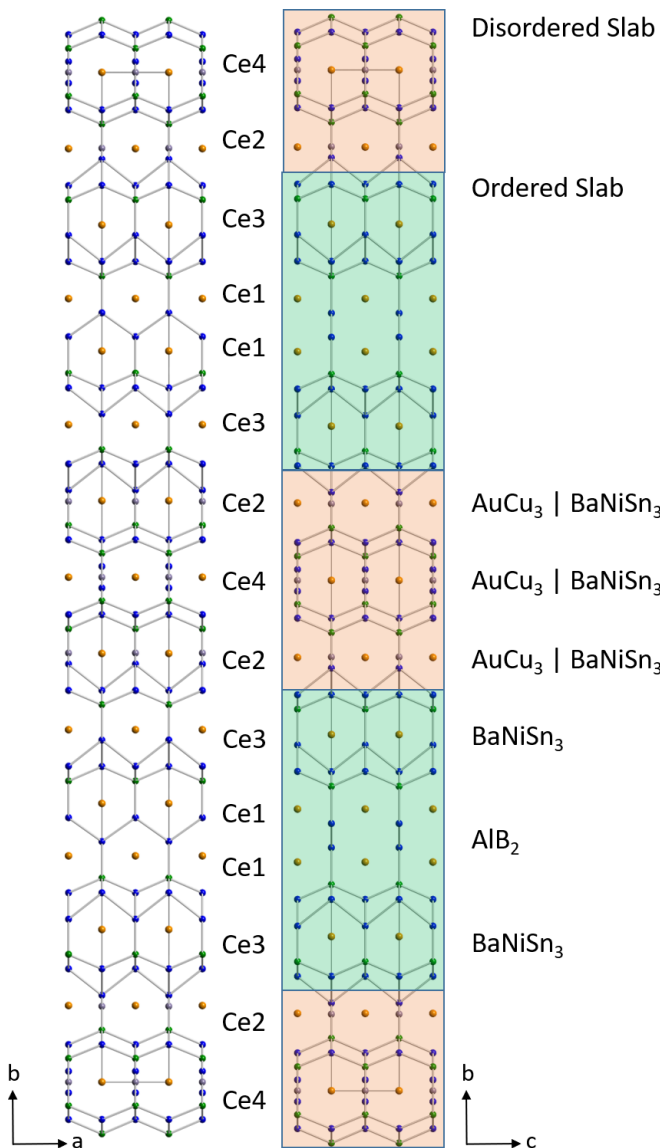
FIG. 2. A projection of the structure of $Ce_7Co_6Ge_{19}$ as viewed down the c axis and the a axis. The ordered Ce1 and Ce3 environments are highlighted in green. The disordered Ce2 and Ce4 environments are highlighted in red. The structural subunits and Ce sites are labeled. Ce atoms are shown as orange spheres, Co as green spheres, and Ge as blue spheres. Sn atoms are shown as grey spheres.

heat capacity was measured for $T = 0.4–100$ K using a Quantum Design physical property measurement system. Electrical resistivity measurements were performed in the same system for $T = 1.8–300$ K in a four-wire configuration.

III. RESULTS

A. Crystal structure

Following the structural pattern of this homologous series where odd n members crystallize in the *Cmcm* space group and even n members crystallize in the *Cmmm* space group [23], the $n = 6$ member is best modeled in the orthorhombic space group *Cmmm*. Figure 2 shows the crystal structure of $Ce_7Co_6Ge_{19}$ along the a and c directions. $Ce_7Co_6Ge_{19}$
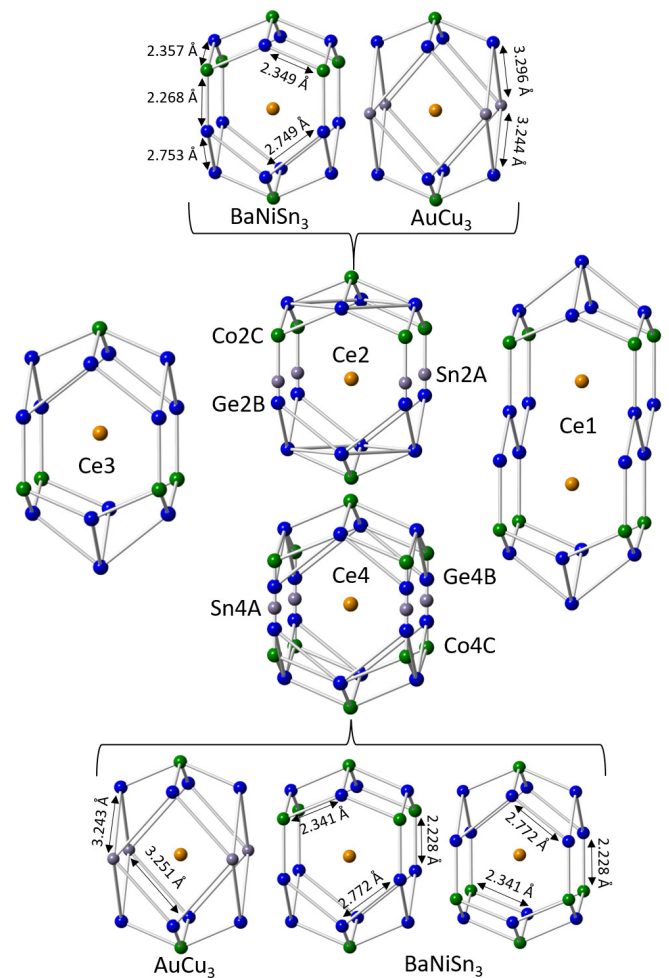
FIG. 3. The local Ce environments in $Ce_7Co_6Ge_{19}$. Ce1 and Ce3 have ordered chemical environments, while Ce2 and Ce4 have disordered environments. For Ce2 and Ce4, the disorder model is shown at the top and bottom of the figure, respectively. Ce is shown in orange, Co in green, Ge in blue, and Sn in grey.

consists of four Ce sites, four Co sites, ten Ge sites, and two Sn sites. The atom assignments were made based on electron density and comparing interatomic distances with those of similar materials, such as $Ln_3Co_{2+x}Ge_{7-y}Sn_y$ ($Ln = $ Pr, Nd, Sm) [15] and $Ce_6Co_5Ge_{16-y}Sn_y$ [18].

Figure 3 shows the Ce local environments. Ce1 is surrounded by eleven Ge atoms and four Co atoms in an AlB_2 orientation. Ce3 of the $BaNiSn_3$-type arrangement, is surrounded by 13 Ge atoms and five Co atoms. The Ce2 local environment is disordered, as is the Ce4 local environment. The positional disorder was made obvious by residual electron density around the equatorial planes of Ce2 and Ce4. The Ce2 unit is $AuCu_3$-type when the Sn2A site is occupied (12.02%) and $BaNiSn_3$-type when Ge2B and Co2C are occupied (87.98%). The Ce4 unit can be $AuCu_3$ when the Sn4A site is occupied (25.30%) or either orientation of the noncentrosymmetric $BaNiSn_3$-subunit when Ge4B and Co4C (74.70%) are occupied, similar to the disordered Pr1 environment in related phase, $Pr_3Co_{2+x}Ge_7$ [15].

The *Cmmm* model showed abnormally high residual electron density and a large wR_2 value. Precession images were
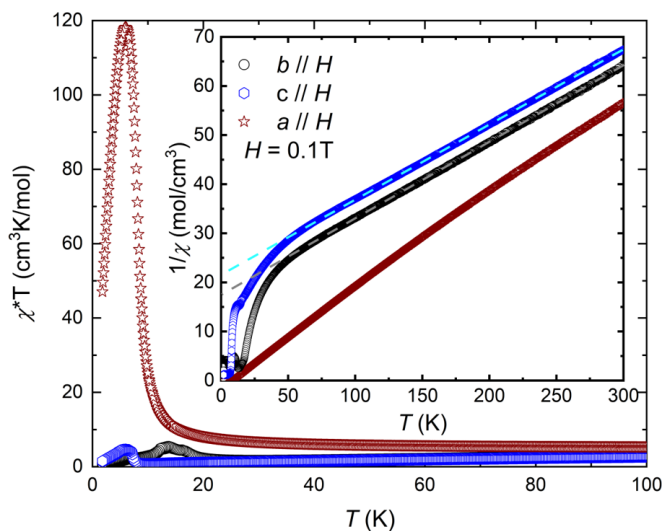
FIG. 4. The evolution of $\chi*T$ vs T shows the strong ferromagnetic fluctuation along the a axis. The inset shows the inverse susceptibility and fit to the Curie-Weiss law (dashed lines).

generated from the data set; images of the $h0l$ plane reveal reflections that are not accounted for by the crystallographic model (Fig. S1). Additional details regarding other attempts to model the data can be found in the Supplemental Material [24]. Although we were not able to obtain a model that accounts for all of the reflections in the $h0l$ precession image, our current best model, described above, is physically reasonable and fits within the greater context of the $A_{n+1}B_nX_{3n+1}$ homologous series.

B. Magnetic and transport properties

The temperature dependent inverse magnetic susceptibility $\chi^{-1}(T)$ data are shown in Fig. 4, where, the overall magnetic anisotropy reveals that the a axis is the easy axis. Above 20 K, the data are described by the Curie-Weiss law $\chi(T) = C/(T - \theta_w)$, where fits to the data yield effective magnetic moments ranging between 2.4 and 2.7μ_B/Ce, similar to the Hund's rule value of 2.54μ_B/Ce for trivalent cerium [25]. The Curie-Weiss constants (θ_w) for a, b, and c directions are 8, -112.5, and -131.7 K, respectively. Strongly negative θ_w values are frequently observed in Ce-containing materials and are often associated with strong hybridization between the f- and conduction-electron states [1]. The additional curvature in $\chi^{-1}(T)$ that is seen at lower temperatures for $H//b$ and c is likely due to a combination of crystal electric field and hybridization effects. The smaller and positive value of θ_w for $H//a$ suggests that in this direction ferromagnetic fluctuations are dominant, but the fact that this is the easy axis also contributes to the differences from the other directions. The evolution of $\chi*T$ vs T is shown in the main panel of Fig. 4, where the values for all three axes increase with decreasing T, which is also consistent with dominant ferromagnetic fluctuations.

At low temperatures, Ce$_7$Co$_6$Ge$_{19}$ has five magnetic phase transitions (Fig. 5). Starting from the paramagnetic state, it first goes through two phase transitions ($T_1 \sim 16.5$ K and $T_2 \sim 12.4$ K) that are evident in the heat capacity as weak
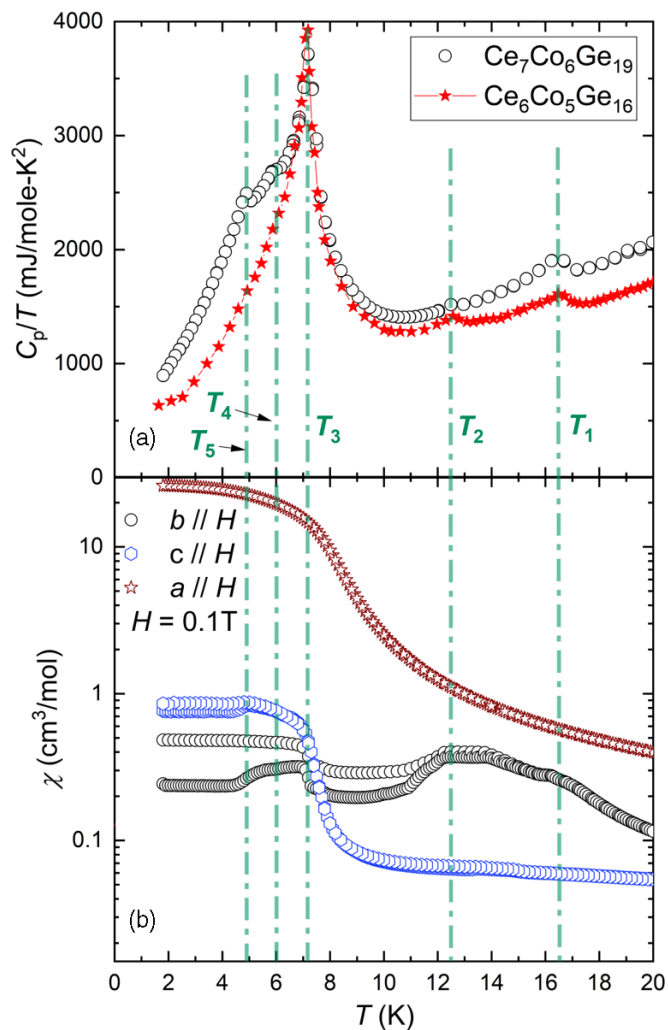
FIG. 5. The five magnetic transitions observed in Ce$_7$Co$_6$Ge$_{19}$. The transition temperatures are highlighted by green dot-dashed lines. (a) C_p/T for Ce$_6$Co$_5$Ge$_{16}$ ($n = 5$) and Ce$_7$Co$_6$Ge$_{19}$ ($n = 6$). Transitions T_1–T_3 occur for both phases. (b) The oriented magnetic susceptibility of Ce$_7$Co$_6$Ge$_{19}$ ($n = 6$). Transitions T_4 and T_5 occur only for $n = 6$.

peaks, indicating that they represent phase transitions that release only a small fraction of the magnetic entropy. These transitions appear as weak shoulders that suppress $\chi(T)$ to values below the extrapolated Curie-Weiss behavior for $H//b$ and c. In contrast, they are not obvious for $\chi(T)$ for H along the a axis. These features are followed by the dominant phase transition at $T_3 \sim 7.2$ K, where there is a large peak in C/T and $\chi(T)$ increases for all applied field directions. This is consistent with coalignment of spins in a quasiferromagnetic arrangement. Finally, there are two additional transitions at $T_4 \sim 6$ K and $T_5 \sim 5$ K that produce weak peaks in C/T, and result in no change in $\chi(T)$ for $H//a$. These features are associated with hysteretic kinks in $\chi(T)$ for $H//b$, c, suggesting that they are minor spin reconfigurations. The field dependent magnetization data are summarized in Fig. 6, where hysteretic s-shaped curves are observed within the ordered states, consistent with the formation of magnetic domains due to ferromagnetic like ordering. For $H//b$ and
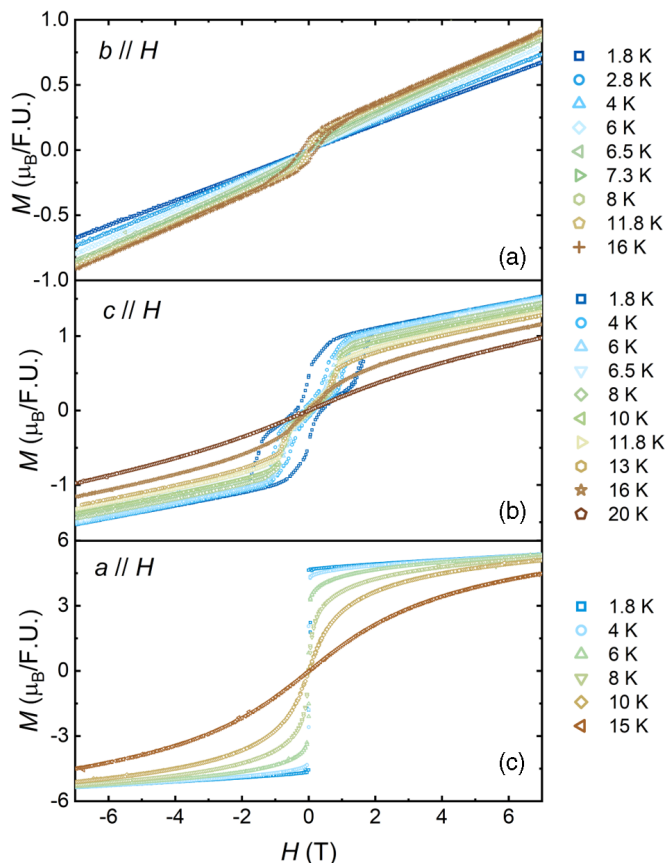
FIG. 6. (a)–(c) Magnetization as a function of field of $Ce_7Co_6Ge_{19}$ performed along all three crystallographic directions at various temperatures. The large magnetization in the *a* direction as compared to the other orientations confirms that this is the magnetic easy axis.

c, $M(H)$ is nonsaturating up to 7 T, which is consistent with our assignment of *b* and *c* as the hard axes. In contrast, for $H//a$ $M(H)$ rapidly saturates towards a value of $5.5\mu_B$/F.U. $(0.785\mu_B$/Ce), which is similar to what is seen for other cerium based intermetallics where a combination of crystal electric field spitting and Kondo hybridization reduces the low temperature moment from the full Hund's rule saturation moment $M_s = g_J J$ ($g_J = 6/7$ and $J = 5/2$).

Further neutron scattering measurements are needed to fully understand this complex magnetic ordering, but it is of interest to note several things. First, we point out that the first three transitions (T_1, T_2, and T_3), are similar to those that are present in the $n = 5$ analog [18]; this may suggest that they arise from the parts of the Ce sublattice that are common to both $n = 5$ and $n = 6$ variants. We also point out that several binary Ce-Ge compounds have ordering temperatures that nearly match ones that are seen here, implying a connection between the magnetism of the subunits and the collective magnetism of the layered compound. This includes; (i) $CeGe_3$, of the $AuCu_3$ structure type, orders antiferromagnetically at $T_N = 12$ K (similar to T_2) [26] and (ii) $CeGe_2$, of the $ThSi_2$ structure type (which is related to AlB_2), orders ferromagnetically at $T_c = 7$ K, (similar to T_3) [27].

In order to clarify the low temperature magnetic and electronic behavior, we isolated the $4f$ heat capacity C_{4f}/T [Fig. 7(b)] by subtracting a phonon term, which was modeled using the Debye function for temperatures above the ordered state (Fig. 7 dashed line). This fit yields a Debye temperature $\Theta_D = 236$ K, which is comparable to that seen for many other related Ce-Ge compounds. In addition to the magnetic ordering, the resulting C_{4f}/T curve shows a tendency for the underlying electronic term to increase with decreasing temperature to reach a value near $g = 760$ mJ/mol K^2 (108 mJ/mol-Ce K^2) approaching zero temperature. This reveals (i) a possible deviation from simple Fermi liquid behavior and (ii) that the charge carrier quasiparticles have an enhanced mass, similar to what is seen for other cerium based heavy fermion materials [1,3,28]. By integrating C_{4f}/T we obtain $S_{4f}(T)$ [Fig. 7(c)], which reaches $0.57R$ ln2 (per cerium) at T_1. A significant fraction of this entropy is recovered at T_3, consistent with our assignment of T_3 as the dominant phase transition, while all other transitions represent minor spin reconfigurations. A close inspection of the difference between $C(T)$ and the Debye fit further shows that these curves eventually merge at $T > T_1$, indicating that magnetic fluctuations extend to temperatures above the ordered state and possibly as high as 30 K. This is consistent with there being some magnetic frustration that distributes magnetic entropy to higher temperatures. This also agrees with the view that the five distinct spin reorientation temperatures exist because their associated ground state energies are nearly equal to each other. Finally, we note that even if the additional entropy is considered, $S_{4f}(T)$ only reaches $0.7R$ ln2 per cerium by 30 K. This value is still reduced from the expected value for a ground state doublet and supports the view that there is strong hybridization between the f- and conduction-electron states that results in Kondo screening of the crystal electric field split trivalent cerium moment [1,3,28].

The temperature dependent electrical resistivity, $\rho(T)$, for a $Ce_7Co_6Ge_{19}$ single crystal with the electrical current passing in the *a-c* plane is shown in Fig. 8. The behavior is typical for many Ce-containing compounds, including $CeRhIn_5$ [4], $CePd_2P_2$ [29], and $CeNi_2X_2$ (X = Sb, As, P) [30], and is consistent with expectations for a Kondo lattice [1,3]. In particular, ρ initially weakly decreases with decreasing temperature and eventually evolves through a broad shoulderlike feature at low temperatures that may be due to the removal of scattering channels as the Kondo coherent state forms at low temperatures. In order to investigate whether the saturation mechanism for the scattering at high temperatures is instead due to the breakdown of electrical conduction owing to the electronic mean free path approaching the atomic spacing, we calculated the Ioffe-Regel limit $\sigma_{min} = 0.33e^2/$h-bar $* a$ [31], where e is the electron charge, h-bar is Planck's constant divided by 2*pi and *a* is the lattice constant in the *a-c* plane. From this, we estimate a saturation resistivity near 540 $\mu\Omega$ cm, which is roughly three times the experimental value at 300 K. This suggests that the system is well outside of the Ioffe-Regel limit over the entire measured temperature range. At low temperatures, the magnetic ordering reduces the electronic scattering at T_1, T_2, and T_3, while the drop in resistivity at 3.5 K is most likely due to Sn inclusions. The residual resistivity (ρ_0) is relatively large (42 $\mu\Omega$ cm at 1.8 K), result-
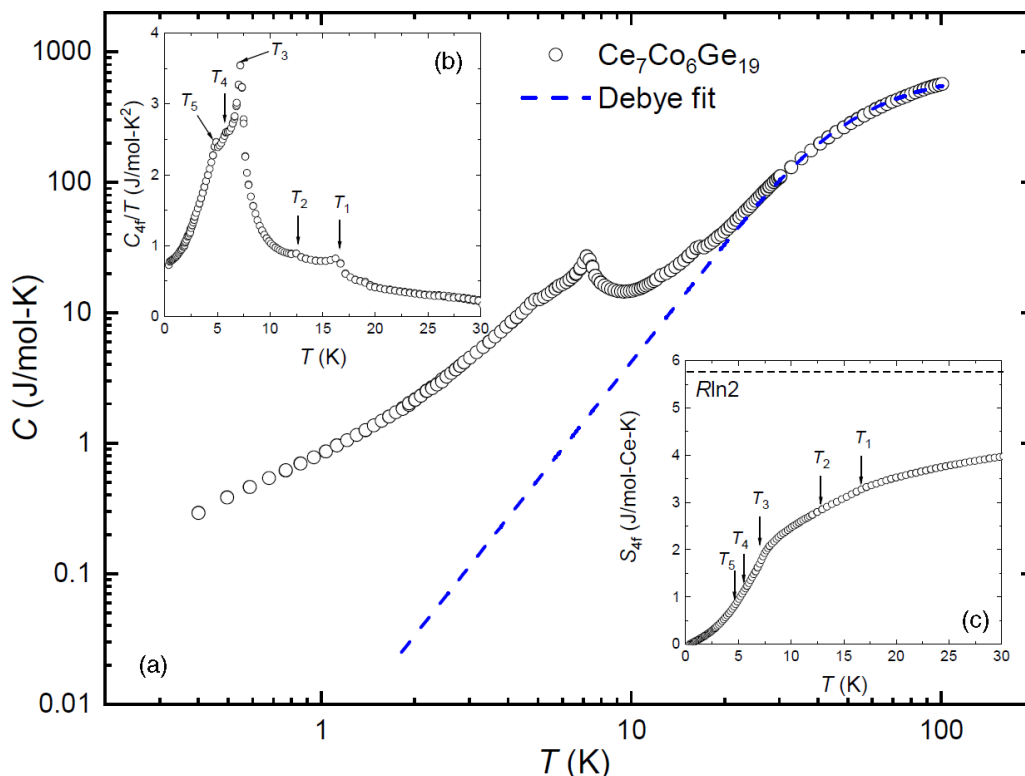
FIG. 7. (a) The temperature dependence of the heat capacity $C(T)$ shown on a log-log plot. The dashed blue line represents a Debye fit to the data, as described in the text. (b) The $4f$ contribution to the heat capacity divided by temperature C_{4f}/T vs T, which was isolated as described in the text. The ordering temperatures are indicated by arrows. (c) The temperature dependent entropy of the magnetic Ce $4f$ electrons $S_{4f}(T)$.

ing in a residual resistivity ratio (RRR) of 3.6. Both the ρ_0 and the RRR values indicate a significantly disordered environment, consistent with the positional disorder in $Ce_7Co_6Ge_{19}$, as observed from single crystal X-ray diffraction.

Taken together, these results shows that this structure type is a reservoir for complex magnetism that likely arises from
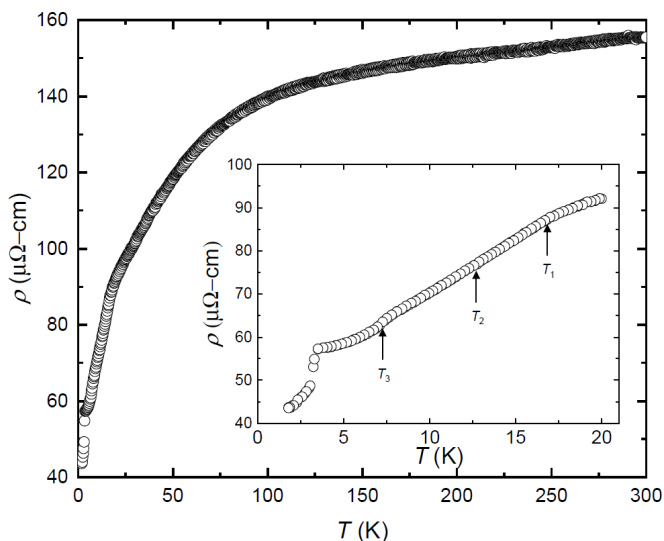
FIG. 8. The electrical resistivity of $Ce_7Co_6Ge_{19}$. The inset shows the low temperature region (below 20 K), where the ordering temperatures are marked by arrows.

(i) an interplay between there being several distinct Ce sites with different dominant spin interactions and (ii) the occurrence of Kondo hybridization between the f- and conduction-electron states. Evidence for the latter is seen in the Kondo coherence behavior of the electrical resistivity, the enhanced value of the electronic coefficient of the heat capacity, and the suppressed value of the $4f$ entropy. At the same time, the magnetic ordering is complex, showing five distinct phase transitions that are seen as bulk features in the heat capacity, the magnetic susceptibility, and the electrical resistivity. The dominant phase transition at T_3 results in a strong increase in $\chi(T)$ for $H // a$, which implies a net ferromagnetic alignment of spins. However, the complexity that is seen for the other directions makes it clear that this is not simple ferromagnetism, and there are several spin reconfigurations over a small temperature range. Further neutron scattering measurements are needed to understand the ordered states. Together with the long tail of residual entropy that extends to temperatures above T_1, this suggests that there are several competing magnetic exchange interactions that are similar in energy; i.e., the system is magnetically frustrated. Even in simple lattices with only a single cerium site, there is potential for magnetic frustration that results from differences between nearest neighbor and next nearest neighbor magnetic exchanges that are mediated by the RKKY interactions [32,33] (e.g., as for the anisotropic next nearest neighbor interaction ANNNI model [34]). We speculate that this, together with the multiple distinct cerium sites and the added influence of the

Kondo hybridization, contributes to the magnetic complexity of this system.

IV. CONCLUSIONS

Similar to $Ce_6Co_5Ge_{16}$ ($n = 5$), the stacking of structural subunits in $Ce_7Co_6Ge_{19}$ ($n = 6$) creates a rich environment in which to study the interactions of Ce $4f$ and conduction electrons. The relationship between $n = 5$ and $n = 6$ is evident given the three kindred magnetic transitions that are present in both compounds. The additional disordered subunits in $n = 6$ adds significant complexity to the crystal structure giving rise to two further magnetic transitions. We have shown that the physical properties of complex materials are correlated with the properties of constituent structural subunits. The "bulk heterostructural" single crystal growth of not just a different structure type, but also a robust series, can potentially bring the goal of the rational design of quantum materials closer to fruition.

[1] G. R. Stewart, Heavy-fermion systems, Rev. Mod. Phys. **56**, 755 (1984).

[2] H. v. Löhneysen, A. Rosch, M. Vojta, and P. Wölfle, Fermi-liquid instabilities at magnetic quantum phase transitions, Rev. Mod. Phys. **79**, 1015 (2007).

[3] C. Pfleiderer, Superconducting phases of f-electron compounds, Rev. Mod. Phys. **81**, 1551 (2009).

[4] H. Hegger, C. Petrovic, E. G. Moshopoulou, M. F. Hundley, J. L. Sarrao, Z. Fisk, and J. D. Thompson, Pressure-Induced Superconductivity in Quasi-2D CeRhIn$_5$, Phys. Rev. Lett. **84**, 4986 (2000).

[5] N. apRoberts-Warren, A. P. Dioguardi, A. C. Shockley, C. H. Lin, J. Crocker, P. Klavins, and N. J. Curro, Commensurate antiferromagnetism in CePt$_2$In$_7$, a nearly two-dimensional heavy fermion system, Phys. Rev. B **81**, 180403 (2010).

[6] C. Petrovic, P. G. Pagliuso, M. F. Hundley, R. Movshovich, J. L. Sarrao, J. D. Thompson, Z. Fisk, and P. Monthoux, Heavy-fermion superconductivity in CeCoIn$_5$ at 2.3 K, J. Phys.: Condens. Matter **13**, L337 (2001).

[7] J. L. Sarrao, L. A. Morales, J. D. Thompson, B. L. Scott, G. R. Stewart, F. Wastin, J. Rebizant, P. Boulet, E. Colineau, and G. H. Lander, Plutonium-based superconductivity with a transition temperature above 18 K, Nature (London) **420**, 297 (2002).

[8] D. Aoki, Y. Haga, D. T. Matsuda, N. Tateiwa, S. Ikeda, Y. Homma, H. Sakai, Y. Shiokawa, E. Yamamoto, A. Nakamura, R. Settai, and Y. Ōnuki, Unconventional heavy-fermion superconductivity of a new transuranium compound NpPd$_5$Al$_2$, J. Phys. Soc. Jpn. **76**, 063701 (2007).

[9] A. Weiland, J. B. Felder, G. T. McCandless, and J. Y. Chan, One Ce, Two Ce, Three Ce, Four? An intermetallic homologous series to explore: $A_{n+1}B_nX_{3n+1}$, Chem. Mater. **32**, 1575 (2020).

[10] O. I. Bodak and E. I. Gladyshevskii, Crystal structure of CeNiSi$_2$ and related compounds, Kristallografiya **14**, 990 (1969).

[11] V. K. Pecharsky and K. A. Gschneidner, CeCoGe: A heavy-fermion system, Phys. Rev. B **43**, 8238 (1991).

[12] W. Dörrscheidt and H. Schäfer, Darstellung Und Kristallstruktur von BaPdSn, SrPdSn und LaCoSn, J. Less-Common Met. **70**, 1 (1980).

[13] B. Chevalier and J. Etourneau, Antiferromagnetic properties of the intermetallics Ce$_3$Ni$_2$X$_7$ (X = Geor Sn), J. Mater. Chem. **9**, 1789 (1999).

[14] X. Lin, S. L. Bud'ko, S. Thimmaiah, and P. C. Canfield, Anisotropic magnetization, resistivity and heat capacity of single crystalline R_3Ni$_{2−x}$Sn$_7$ (R = LaCe, Pr and Nd), J. Magn. Magn. Mater. **331**, 53 (2013).

[15] M. A. Khan, G. T. McCandless, K. A. Benavides, T. J. Martin, A. M. Palacios, A. W. B. Samuel, D. P. Young, and J. Y. Chan, Crystal growth and magnetic properties of Pr$_3$Co$_{2+x}$Ge$_7$ and the Sn-stabilized Ln_3Co$_{2+x}$Ge$_{7−y}$Sn$_y$ (Ln = Pr, Nd, Sm), Cryst. Growth. Des. **18**, 6028 (2018).

[16] T. Hermening, M. Eul, and R. Pottgen, Nickel-deficient stannides Eu$_2$Ni$_{2−x}$Sn$_5$-structure, magnetic properties, and moessbauer spectroscopic characterization, Z. Naturforsch. **64**, 1107 (2009).

[17] B. Belan, J. Stepen-Damm, R. Gladyshevskii, and O. Bodak, The new structure type Ce$_5$Co$_4$Ge$_{13}$, Chem. Met. Alloys **1**, 43 (2008).

[18] J. B. Felder, A. Weiland, H. Hodovanets, G. T. McCandless, T. G. Estrada, T. J. Martin, A. V. Walker, J. Paglione, and J. Y. Chan, Law and disorder: Special stacking units—building the intergrowth Ce$_6$Co$_5$Ge$_{16}$, Inorg. Chem. **58**, 6037 (2019).

[19] P. C. Canfield, T. Kong, U. S. Kaluarachchi, and N. H. Jo, Use of Frit-Disc crucibles for routine and exploratory solution growth of single crystalline samples, Philos. Mag. **96**, 84 (2016).

[20] L. Krause, R. Herbst-Irmer, G. M. Sheldrick, and D. Stalke, Comparison of silver and molybdenum microfocus X-ray sources for single-crystal structure determination, J. Appl. Crystallogr. **48**, 3 (2015).

[21] G. M. Sheldrick, SHELXT–Integrated space-group and crystal-structure determination, Acta Crystallogr. A. **71**, 3 (2015).

[22] G. M. Sheldrick, Crystal structure refinement with SHELXL, Acta Crystallogr. C **71**, 3 (2015).

[23] K. A. Benavides, L. J. Treadwell, R. N. McDougald, G. D. Campbell, G. T. McCandless, and J. Y. Chan, Structural stability and magnetic properties of LnM_xGa_3 (Ln = Ho, Er;M = Fe, Co;$x < 0.2$), Polyhedron **114**, 56 (2016).

[24] See Supplemental Material at http://link.aps.org/supplemental/10.1103/PhysRevMaterials.4.074408 for additional details regarding our attempts to model the crystal structure.

[25] N. W. Ashcroft and N. D. Mermin, *Solid State Physics* (Saunders, Philadelphia, 1976).

[26] F. Hiroshi and Y. Shoji, High-pressure synthesis and properties of a cerium germanide $CeGe_3$ with the cubic Cu_3Au type structure, Chem. Lett. **33**, 1334 (2004).

[27] H. Yashima, T. Satoh, H. Mori, D. Watanabe, and T. Ohtsuka, Thermal and magnetic properties and crystal structures of $CeGe_2$ and $CeSi_2$, Solid State Commun. **41**, 1 (1982).

[28] G. R. Stewart, Non-Fermi-liquid behavior in d- and f-electron metals, Rev. Mod. Phys. **73**, 797 (2001).

[29] V. H. Tran and Z. Bukowski, Ferromagnetism in the Kondo-lattice compound $CePd_2P_2$, J. Phys.: Condens. Matter **26**, 255602 (2014).

[30] H. Suzuki, H. Abe, H. Kitazawa, and D. Schmitt, Magnetic properties and resistivity of ternary compounds $CeNi_2X_2$ (X = Sb, As, P), J. Alloys Compd. **323–324**, 520 (2001).

[31] M. Gurvitch, Ioffe-Regel criterion and resistivity of metals, Phys. Rev. B **24**, 7404 (1981).

[32] R. E. Baumbach, H. Chudo, H. Yasuoka, F. Ronning, E. D. Bauer, and J. D. Thompson, CeRuAlB: A local-moment $4f$ magnet with a complex T-H phase diagram, Phys. Rev. B **85**, 094422 (2012).

[33] K. W. Chen, Y. Lai, Y. C. Chiu, S. Steven, T. Besara, D. Graf, T. Siegrist, T. E. Albrecht-Schmitt, L. Balicas, and R. E. Baumbach, Possible devil's staircase in the Kondo lattice CeSbSe, Phys. Rev. B **96**, 014421 (2017).

[34] W. Selke and P. M. Duxbury, The mean field theory of the three-dimensional ANNNI model, Z.Phys. **57**, 49 (1984).